Accepted Manuscript

Neutron-irradiation creep of silicon carbide materials beyond the initial transient

Takaaki Koyanagi, Yutai Katoh, Kazumi Ozawa, Kazuya Shimoda, Tatsuya Hinoki, Lance L. Snead

PII: S0022-3115(16)30257-4

DOI: 10.1016/j.jnucmat.2016.06.006

Reference: NUMA 49759

To appear in: *Journal of Nuclear Materials*

Received Date: 11 January 2016

Revised Date: 26 May 2016

Accepted Date: 2 June 2016

Please cite this article as: T. Koyanagi, Y. Katoh, K. Ozawa, K. Shimoda, T. Hinoki, L.L. Snead, Neutron-irradiation creep of silicon carbide materials beyond the initial transient, *Journal of Nuclear Materials* (2016), doi: 10.1016/j.jnucmat.2016.06.006.

Title: Neutron-irradiation creep of silicon carbide materials beyond the initial transient

Authors: Takaaki Koyanagi,[1] Yutai Katoh,[1] Kazumi Ozawa,[2] Kazuya Shimoda,[3] Tatsuya Hinoki,[3] Lance L. Snead[4]

Affiliation:
1. Oak Ridge National Laboratory, Oak Ridge, Tennessee 37831, USA
2. Japan Atomic Energy Agency, Rokkasho, Aomori 039-3212, Japan
3. Institute of Advanced Energy, Kyoto University, Kyoto 611-0011, Japan
4. Massachusetts Institute of Technology, Cambridge, Massachusetts

Contact Author: Takaaki KOYANAGI

Materials Science and Technology Division
Oak Ridge National Laboratory
1 Bethel Valley Road, A-154 Building 4500S
Oak Ridge, TN 37831-6140 USA

Email: koyanagit@ornl.gov
TEL: +1-865-574-8764
Fax: +1-865-241-3650

Neutron-irradiation creep of silicon carbide materials beyond the initial transient[i]

Abstract

Irradiation creep beyond the transient regime was investigated for various silicon carbide (SiC) materials. The materials examined included polycrystalline or monocrystalline high-purity SiC, nanopowder sintered SiC, highly crystalline and near-stoichiometric SiC fibers (including Hi-Nicalon Type S, Tyranno SA3, isotopically-controlled Sylramic and Sylramic-iBN fibers), and a Tyranno SA3 fiber–reinforced SiC matrix composite fabricated through a nano-infiltration transient eutectic phase process. Neutron irradiation experiments for bend stress relaxation tests were conducted at irradiation temperatures ranging from 430 to 1180°C up to 30 dpa with initial bend stresses of up to ~1 GPa for the fibers and ~300 MPa for the other materials. Initial bend stress in the specimens continued to decrease from 1 to 30 dpa. Analysis revealed that (1) the stress exponent of irradiation creep above 1 dpa is approximately unity, (2) the stress normalized creep rate is ~1×10^{-7} [$dpa^{-1}MPa^{-1}$] at 430 to 750°C for the range of 1 to 30 dpa for most polycrystalline SiC materials, and (3) the effects on irradiation creep of initial microstructures—such as grain boundary, crystal orientation, and secondary phases—increase with increasing irradiation temperature.

1. Introduction

Irradiation creep is an important phenomenon for nuclear materials because of its potential impact on the design stresses and service lifetimes of thermo-structural components. For silicon carbide (SiC) and SiC fiber–reinforced SiC matrix (SiC/SiC) composites, irradiation creep is also known to be a key property in defining design windows [1, 2]. In short, and especially for materials such as SiC and its composites that possess very limited strain tolerance, irradiation creep provides an important stress mitigating function.

The irradiation creep of SiC under various neutron irradiation conditions was investigated on monolithic forms fabricated by chemical vapor deposition (CVD) [3, 4, 5] and by hot-pressing of a SiC nanopowder [6]. These studies found transient irradiation creep in SiC for conditions under which thermal creep was negligible. The transient irradiation creep of CVD SiC is well explained as a consequence of anisotropic swelling due to applied stresses [5]. In contrast, the initial irradiation creep of hot-pressed SiC materials is affected by secondary phases at the grain boundaries and in grain pockets [6].

Although transient irradiation creep of SiC is understood, higher-dose irradiation creep behavior is not as clear. Previous studies indicated post-transient creep, i.e. secondary creep, of SiC operating from ~1 dpa [4, 5]. However, there is not enough evidence to prove the presence of secondary creep. In this study, the irradiation creep experiment was extended to a higher neutron fluence using the same method used in the previous work by Katoh et al. [5]. The results show the high-dose irradiation creep behavior of various SiC materials, including grades of CVD SiC materials, nanopowder sintered SiC, nuclear-grade SiC fibers, and an SiC/SiC composite. The neutron irradiation creep of SiC fibers and SiC/SiC composites is poorly understood, although the ion-irradiation creep of SiC fibers such as SCS-6, Sylramic, and Tyranno SA3 fibers has been reported [7-11].

The bend stress relaxation (BSR) technique was originally developed and thoroughly applied by Morscher, et al [12] to study the thermal creep in advanced SiC fiber utilized in composite manufacture. It has become a common technique for measuring irradiation creep of ceramics materials [5]. The BSR method is useful for neutron irradiation experiments because it enables the application of stress on miniature specimens under irradiation, and it requires only a very simple post-irradiation measurement. However, decreasing applied stress during testing and a nonuniform stress state in samples make evaluation difficult in certain conditions. When the applied stress is fully relaxed, further determination of creep behavior is impossible. In a previous study [5], more than 60% of the initial stress was retained in CVD SiC materials following irradiation to ~1 dpa. Thus the investigation of creep at a higher dose is possible for these materials. The other limitation, nonuniform stress in the specimen, can affect the analysis. If the creep rate is linear with the applied stress level and the specimen has a uniform microstructure, the analysis is straightforward and quantitative. If that is not the case, the creep rate obtained and the stress exponent are semi-quantitative. Quantitative analysis of the creep was demonstrated in most cases in this study because the experimental results meet those requirements. However, a relative comparison of creep behavior was used in the evaluation of creep in SiC/SiC composites owing to the nonuniform microstructures.

2. Experimental

2.1 Materials

The materials used were CVD SiC monoliths, nanopowder sintered SiC ceramics, nuclear-grade SiC fibers, and an SiC/SiC composite. Key properties of those materials are summarized in Table 1. The CVD SiC materials include Rohm & Haas (currently Dow Chemical Co., Marlborough, Massachusetts) CVD SILICON CARBIDE high-resistivity grade (RH hereinafter); Coorstek (Hillsboro, Oregon) PureSiC (CT); and monocrystalline, nitrogen-doped Cree 4H–SiC (4H). All three materials were at least >99.999% pure. The CVD materials were annealed in a flowing argon environment at 1900ºC for 1 h before machining. The nanopowder sintered SiC materials were fabricated by hot-pressing of powder mixtures containing SiC nanopowder and a total of 12 or 22.5 wt % oxide additives, such as alumina and yttria. The detailed fabrication conditions are described elsewhere [6]. The hot-pressed SiCs fabricated with 12 and 22.5 wt % additives are called NT1 and NT2, respectively. The SiC/SiC composite was unidirectionally reinforced with Tyranno SA3 SiC fibers (Ube Industries. Ltd., Ube, Japan) with a pyrolytic carbon interface ~500 nm thick deposited on the fiber surface by CVD. The composite material was fabricated via the nano-infiltration transient eutectic (NITE) process [13] with the fibers, SiC nanopowder, and a total 12 wt % Al_2O_3 + Y_2O_3 + SiO_2 additives. The fiber volume fraction was 53%. Details of the fabrication procedure are described elsewhere [14]. The SiC/SiC material was nearly fully dense. The typical Young's modulus, proportional limit stress, and ultimate tensile strength of the composite were ~350 GPa, ~350 MPa, and ~400 MPa, respectively [14]. The CVD SiC, sintered SiC, and SiC/SiC specimens were machined into thin strips with a typical geometry of 40 mm length × 1 mm width × 0.05–0.20 mm thickness and then polished to a mirror finish. The dimensions were slightly changed for selected specimens for identification purpose. For CVD SiC materials, the thickness is parallel to the CVD growth direction. The Cree SiC specimens were machined in an orientation such that the specimen thickness, length, and width directions were parallel to [0001], $[1\bar{1}00]$, and $[11\bar{2}0]$, respectively. The fiber direction in SiC/SiC specimens was parallel to the length of the specimen.

Four SiC fibers were studied: Hi-Nicalon Type S (Nippon Carbon Co., Tokyo, Japan, lot number 407203, March 2005), Tyranno SA3 (Ube Industry Ltd., Tokyo, Japan, type S1I16PX, lot number 4303), experimental-grade Sylramic (COI Ceramics Inc., California, USA, lot number 4240, spool 01A), and experimental-grade Sylramic iBN (COI Ceramics Inc., California, USA, lot number 4630, spool 01B). They are referred to as HNS, SA3, SYL, and SYL-iBN, respectively. Note that the SYL and SYL-iBN fibers tested were isotopically-controlled and mainly contain ^{11}B instead of ^{10}B to avoid boron burnup and

production of transmutant helium by $^{10}B(n, \alpha)^{7}Li$ reactions during irradiation. SYL-iBN fiber is an SYL fiber treated to improve its thermostructural and thermochemical properties by removing the boron from the fiber core region and forming a BN surface coating ~150 nm thick [15].

Table 1. Properties of unirradiated SiC materials

Materials	Alias	Impurity element [wt %]	Young's modulus [GPa]	Average grain size [μm]	Microstructural features
Strip Specimens					
Rohm & Haas CVD	RH	~0	460	~1 [5]	Near-isotropic material
Coorstek CVD	CT	~0	460	~10 [5]	Anisotropic grains. High stacking fault density
Cree CVD	4H	~0	460	N/A	Single crystal
Nanopowder sintered SiC [6]	NT1	12 (Al_2O_3-Y_2O_3-SiO_2)	360	0.4	Secondary phases at grain boundaries
	NT2	22.5 (Al_2O_3-Y_2O_3-SiO_2)	340	0.2	
NITE SiC/SiC composite [14]	SiC/SiC	12 (Al_2O_3-Y_2O_3-SiO_2)	358	0.2	Unidirectionally reinforced composites
Fiber specimens					
Hi-Nicalon Type S	HNS	1.4 C, 0.2 O	420	~0.02 [16]	Fiber diameter: 12 μm Secondary phases at grain boundaries
Tyranno SA3	SA3	2.3 C, <1 O, <1 Al	380	~0.2 [16]	Fiber diameter: 7.5 μm Secondary phases at grain boundaries
Sylramic	SYL	0.8 O, 2.3 ^{11}B, 0.4 N, 2.1 Ti	372	~0.2*[1]	Fiber diameter: 10 μm Secondary phases at grain boundaries
Sylramic iBN	SYL-iBN	0.8 O, 2.3 ^{11}B, 0.4 N, 2.1 Ti	380	~0.2*[1]	Fiber diameter: 10 μm Secondary phases at grain boundaries

Data were obtained from vender or manufacturer unless otherwise indicated.

*[1] Data obtained in this study.

2.2 Bend stress relaxation test

Two fixture types were used for the BSR experiment, one for bulk strip specimens and the other for fiber specimens. The bulk strips were loaded into a fixture with a curvature radius of 100–250 mm to apply flexural stress and then were irradiated. The fixture was fabricated from RH CVD SiC to avoid chemical reactions between the thin strips and the fixture. The initial flexural stress was up to ~300 MPa, depending on the specimen thickness, curvature

radius of the fixture, and modulus of the specimen. The appearances of the specimens and fixtures can be seen in reference [5]. The SiC fiber bundles were loaded into a fixture with three different curvature radii of 2, 3, and 6 mm to apply flexural stress, as shown in Fig. 1, and then were irradiated. Note that intact, unirradiated fibers were straight and did not twist and turn. The fixture was fabricated from nuclear-grade graphite to avoid chemical reactions between fibers and fixture. The initial bending stress levels systematically ranged from ~200 to ~1,100 MPa.

Relaxation creep was evaluated using the BSR ratio (m), which is the ratio of final stress (σ_a) to initial stress (σ_0). The BSR ratio can be expressed as follows:

$$m = \frac{\sigma_a}{\sigma_0} = \frac{E_a(\varepsilon_0 - \varepsilon_c)}{E_0\varepsilon_0} = \frac{E_a}{E_0}\left(1 - \frac{R_a}{R_0}\right) \quad , \tag{1}$$

where E, ε, and R are the elastic modulus, flexural strain, and curvature radius of the specimen, respectively. The subscripts a, 0, and c stand for the initial state, final state, and creep, respectively. The BSR ratio varies between 0 for complete relaxation and 1 for no relaxation. The effect of irradiation on the Young's modulus is assumed to be the same as for CVD SiC [17]. The BSR ratio was evaluated by measuring the curvature radius of the specimen. The curvature radii before and after irradiation were obtained via analysis of the images produced using a KEYENCE, VHX-1000 optical microscope. The creep strain was obtained from the BSR ratio and initial flexural strain from Eq. (1). The stress exponent (n) is expressed by

$$\frac{\varepsilon_c}{\gamma} = A\varepsilon_0^n \quad , \tag{2}$$

where γ is fluence and A is a constant. Further details about BSR testing procedures can be found elsewhere [5, 12]. Irradiation and thermal creep experiments were conducted in an inert-gas atmosphere.

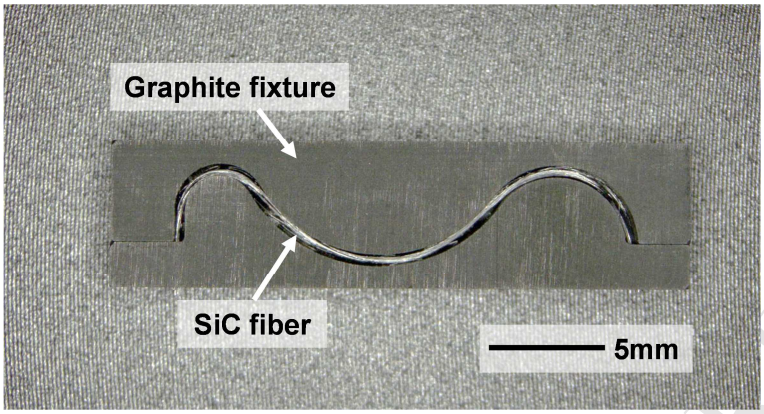

Fig. 1. BSR test fixture and SiC fiber bundles.

2.3 Neutron irradiation

Neutron irradiation occurred in the High-Flux Isotope Reactor (HFIR) at Oak Ridge National Laboratory. The specimens were irradiated at 430 to 1,180°C to 0.97 to 31 dpa-SiC using the conversion factor of 1 dpa = 1.0×10^{25} n/m^2 (E > 0.1 MeV). The damage rate was ~1×10^{-6} dpa/s. The irradiation temperature was determined by measuring the dimensional changes of the RH CVD SiC internal components of the rabbit capsules upon annealing, using a dilatometer. As those SiC parts were designed to be in direct contact with the BSR specimens or BSR fixture during irradiation, this measurement gives an accurate sample temperature during irradiation. Details of the analysis method can be found elsewhere [18].

2.4 Material characterization

The surface morphology of the SiC fibers was examined with a Hitachi S4700 scanning electron microscope. Phases in the SiC fibers were determined by x-ray powder diffraction (XRD). All the XRD patterns were acquired using a Scintag powder diffractometer and copper K-α radiation (40 kV and 40 mA). The peak position was calibrated using silicon powder as an internal standard. Densities of selected bulk specimens were evaluated by the liquid density column technique following ASTM Standard D1505–10. The density column used a mixture of bromoform and diiodomethane. For the columns utilized in this experiment the estimated accuracy in the density measurement was ~0.0005 g/cm^3. Five pieces of the bulk specimens were evaluated for each irradiation condition. Microstructures of the specimens were examined by transmission electron microscopy (TEM). TEM foils of RH creep specimens were prepared from uniaxially tensile-stressed areas. The bent specimens were first thinned to ~30 μm from the compressive side using mechanical polishing. After that, the specimen was milled using a Fischione model 1010 argon ion mill operated at 3–5 keV. In this process, the tension surface was milled by ~1 μm first, to remove

the layer affected by surface effects. After that, the specimen was thinned from the compressive side. TEM specimens to serve reference specimens and specimens irradiated without stress were prepared using conventional techniques with ion milling or focused ion beam (FEI Versa 3D DualBeam). Irradiation defects were observed using a Philips Tecnai 20 operated at 200 kV. High-resolution imaging and elemental analysis with an energy-dispersive x-ray spectroscope (EDS) were conducted using a JEOL JEM2100F operated at 200 kV.

3. Results

3.1 Characterization of unirradiated materials

Microstructural features of unirradiated SiC materials are summarized in Table 1. RH and CT CVD SiC were investigated in previous work [5]. The CT material showed columnar grains along the CVD direction, and the column width was typically more than a few μm. In addition, the grains were highly faulted. The RH material exhibited a relatively isotropic microstructure with a few μm-sized random grains without significant stacking-fault density. In contrast to RH and CT SiC, few defects were found in 4H SiC; high-resolution TEM imaging (Fig. 2) and the diffraction pattern confirmed that there was only 4H phase in the material, and the number density of defects such as stacking faults was very limited.

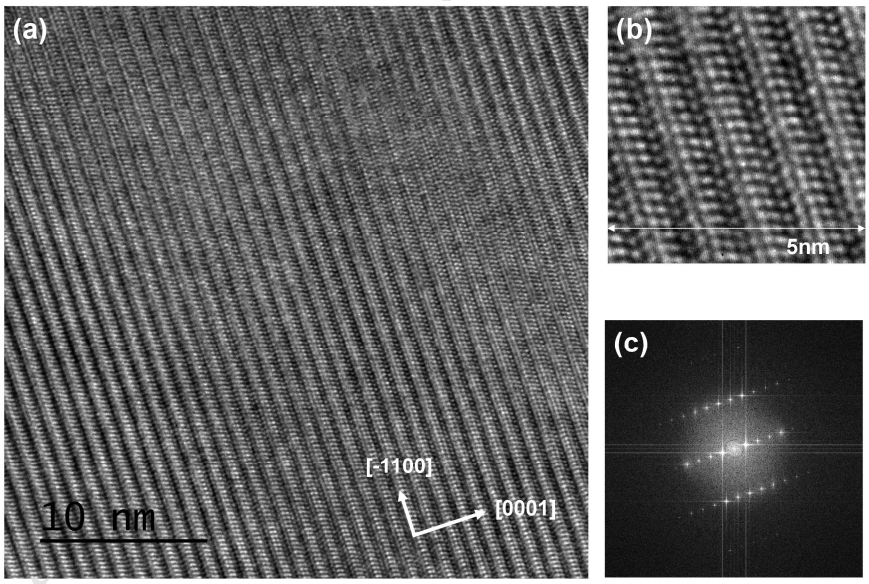

Fig. 2. High-resolution (HR) TEM micrograph of unirradiated 4H SiC (a, b) and fast Fourier transform spectra of the HR TEM micrograph. Image was taken from the [11-20] direction.

XRD patterns of unirradiated fibers are shown in Fig. 3. The main crystalline phase of all the fibers was β-SiC. Shoulder peaks on the low-angle side of the (111) peak of β-SiC near 34°

(2θ) were detected for all the fibers; these are known as disordered peaks, indicating the existence of defects such as stacking faults [19]. The peak at ~44° in SYL and SYL-iBN fibers was identified as the TiB_2 phase. The amount of TiB_2 phase on the analyzed surface of SYL and SYL-iBN fibers was estimated to be 5 wt % for both fibers.

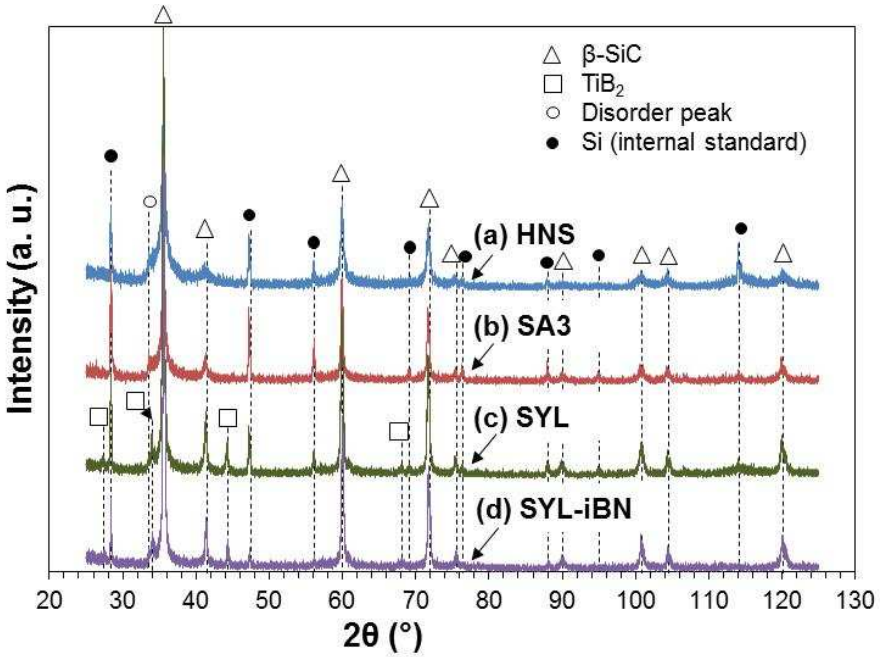

Fig. 3 XRD patterns of unirradiated (a) HNS, (b) SA3, (c) SYL, and (d) SYL-iBN fibers.

Very similar microstructures were observed for SYL and SYL-iBN fibers, except for the presence of a BN phase on the surface of SYL-iBN. TEM micrographs of SYL fiber in the unirradiated condition are shown in Fig. 4. The average grain size was ~200 nm. Scanning TEM imaging and elemental mapping using EDS analysis revealed the presence of titanium and carbon phases at the grain pockets of both fibers. The titanium phase is TiB_2, based on the XRD results. The thickness of the BN layer on the SYL-iBN fiber surface was ~100 nm or less. Microstructures of HNS and SA3 fibers have been reported in a previous study [16]. HNS reportedly consists of nanocrystalline SiC grains (~20 nm) and carbon phases at grain pockets and grain boundaries. SA3 fiber also contains carbon phases. SA3 exhibits a similar grain size to those of SYL and SYL-iBN fibers. In summary, the fiber specimens consist of much smaller grains than CVD SiC and contain secondary phases at the grain boundaries and in grain pockets.

The nanopowder sintered SiC also consists of submicron SiC grains and secondary phases at grain boundaries and triple points. The NT1 and NT2 materials exhibited fine-grain microstructures with average grain sizes of ~400 nm for NT1 and ~200 nm for NT2 [6]. The

secondary phases are attributed to the oxide additives (alumina, yttria, and silica) [6]. The Y-Al-O phases are also found in the NITE SiC/SiC composite. The oxide phases were found both in the matrix-rich areas and segregated to occupy the spaces within the fiber bundles and at the inter-bundle pockets [14].

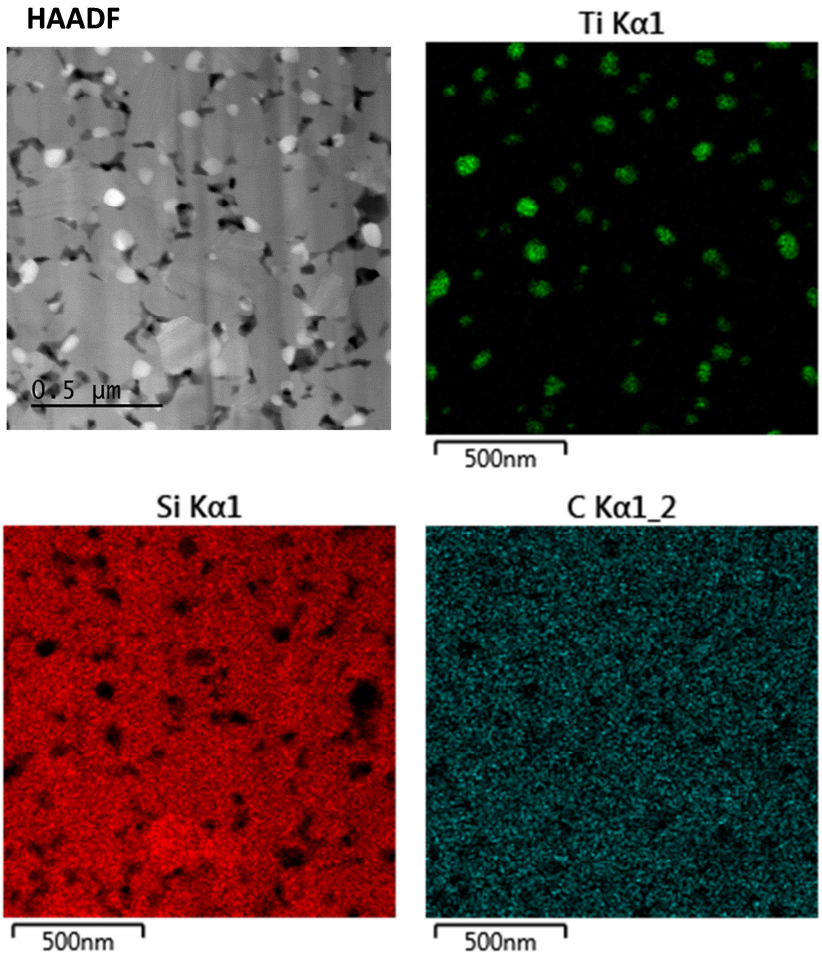

Fig. 4 High-angle annular dark field (HAADF) image and elemental mappings of unirradiated SYL fibers. The black contrast in the HAADF image indicates the presence of free carbon.

3.2 Stress relaxation behavior

Creep deformation of the thin strip specimens could be visually observed in most cases after they were removed from the BSR fixture. Creep deformation was also obvious in the fiber specimens, as shown in Fig. 5. The fiber bundles exhibited creep deformation behaviors depending on the three different initial applied stresses imposed by the different curvatures in the identical specimens.

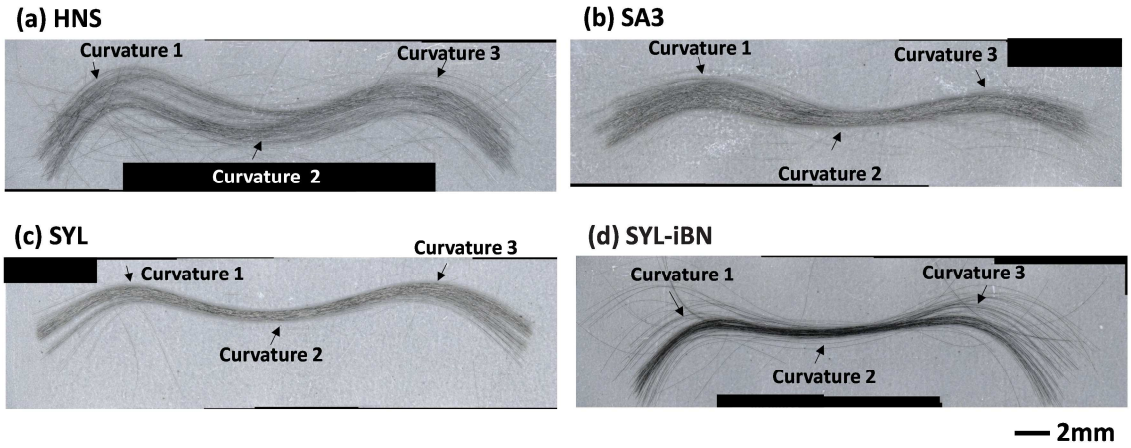

Fig. 5. SiC fibers following BSR experiments under irradiation at 580 °C to 0.97 dpa: HNS (a), SA3 (b), SYL (c), and SYL-iBN (d) fibers. The fibers deformed depending on three different initial applied stresses in the identical specimens. Curvatures 1, 2, and 3 in the images were formed by elastic constraint by the graphite fixture with 2, 6, and 3 mm curvature radii during irradiation, respectively.

The degree of radiation creep of a total of 120 monolithic and composite specimens was evaluated. Their measured BSR ratios are summarized in Table 2. Figure 6 shows BSR ratios of monolithic SiC ceramics and an SiC/SiC composite plotted against the average flexural stress. The horizontal error bars indicate the range of flexural stress during irradiation, with the highest at the beginning of irradiation and the lowest at the end of irradiation. The BSR ratios appeared insensitive to the magnitude of the applied stress unless a limited number of specimens was available for the NT2 and 4H materials at a certain irradiation condition. This indicates that the stress exponent of irradiation creep was approximately unity, according to the analysis of the stress exponent dependence of the BSR ratio based on Eqs. (1) and (2) (Fig. 6d). At 750°C to 29 dpa, RH SiC exhibited BSR ratios with relatively large deviations. This may be caused by differences in the starting microstructure, such as the relationship of grain sizes from specimen to specimen, which is discussed later.

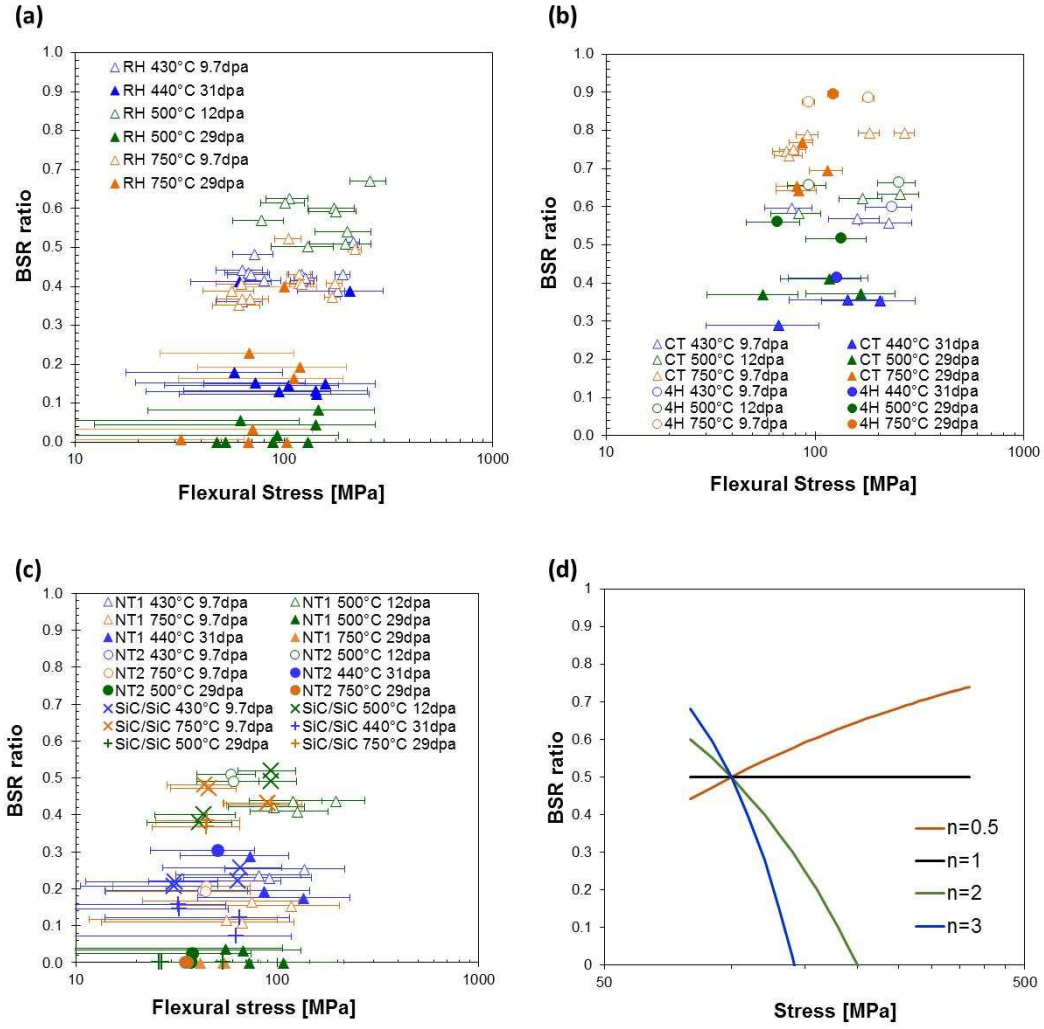

Fig. 6 Effects of applied stress on BSR ratios: RH (a), CT and 4H (b), NT1, NT2 and SiC/SiC (c) materials. Effects of stress and stress exponent (n) on BSR ratio (d) were obtained based on Eqs. (1) and (2).

Table 2. Summary of results for irradiation creep measurements for CVD SiC, sintered SiC, and SiC/SiC composite. Parentheses indicate standard deviations

Material	Irradiation temperature [°C]	Dose [dpa]	Number of test specimens	Range of initial stress [MPa]	Average BSR ratio (standard deviation)
RH	430	9.7	4	97–288	0.43 (0.04)
	440	31.0	9	88–301	0.20 (0.11)
	500	11.6	4	101–313	0.58 (0.06)
	500	29.0	9	97–278	0.02 (0.03)
	750	9.7	4	84–303	0.41 (0.05)
	750	29.0	8	66–213	0.13 (0.14)
CT	430	9.7	3	98–295	0.57 (0.02)
	440	31.0	3	105–307	0.33 (0.04)
	500	11.6	3	213–320	0.63 (0.01)
	500	29.0	3	84–246	0.38 (0.02)
	750	9.7	3	86–106	0.75 (0.02)
	750	29.0	4	101–140	0.69 (0.06)
4H	430	9.7	1	88–175	0.60
	440	31.0	1	182	0.41
	500	11.6	2	114–306	0.66 (0.03)
	500	29.0	2	85–178	0.54 (0.03)
	750	9.7	2	103–197	0.88 (0.01)
	750	29.0	1	133	0.89
NT1	430	9.7	3	134–221	0.24 (0.01)
	440	31.0	3	116–233	0.22 (0.06)
	500	11.6	4	139–278	0.43 (0.01)
	500	29.0	4	109–220	0.02 (0.02)
	750	9.7	4	105–213	0.14 (0.03)
	750	29.0	3	87–115	0.00 (0.00)

NT2	430	9.7	1	73	0.19
	440	31.0	1	79	0.41
	500	11.6	2	80–83	0.50 (0.02)
	500	29.0	2	76–77	0.01 (0.02)
	750	9.7	2	77	0.20 (0.01)
	750	29.0	2	74–75	0.00 (0.00)
SiC/SiC	380	1.5	4	56–113	0.68 (0.05)
	430	9.7	4	51–107	0.23 (0.02)
	440	31.0	4	57–119	0.12 (0.04)
	500	11.6	4	61–127	0.45 (0.07)
	500	29.0	4	53–110	0.00 (0.00)
	750	9.7	4	61–130	0.45 (0.03)
	750	29.0	3	67–137	0.39 (0.03)

More than 200 locations in the fibers were evaluated in the creep experiments. The results are summarized in Table 3, and the stress dependence of the BSR ratios of the SiC fibers is shown in Fig. 7. Based on the analysis of the effects of the stress exponent on the BSR ratio, e.g., Fig. 6d, the stress exponents of the irradiated fibers ranged between 0.5 and 1.5 and were slightly lower than unity in most cases. This result also applied for the stress exponents of thermal creep. A similar order of creep strain was observed between the thermal creep for 240 h and the irradiation creep for 0.97 dpa at ~1200°C. The exposure time of irradiation to 0.97 dpa corresponded to ~240 h in this study, and creep under irradiation can be significantly affected or dominated by thermal creep at such a high temperature.

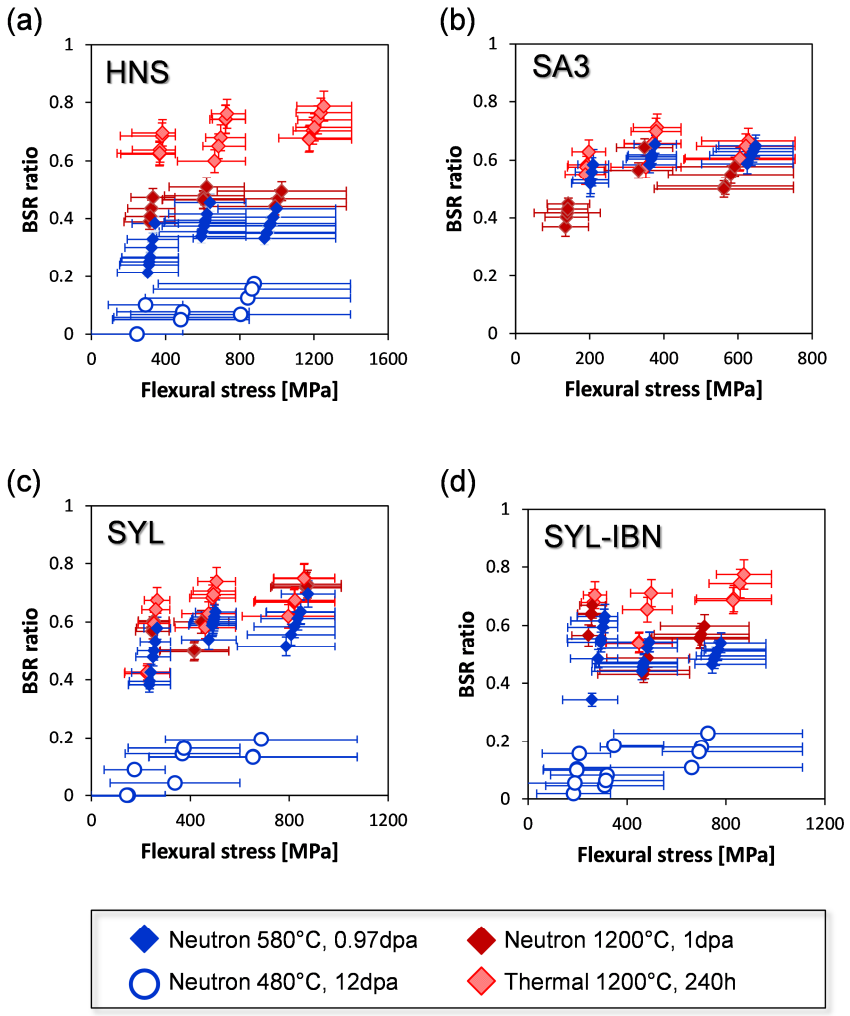

Fig. 7 Stress dependence of BSR ratios for irradiation and thermal creep experiments on SiC fibers: HNS (a), SA3, (b), SYL (c), and SYL-iBN (d). The highest and lowest values of the error bars indicate the initial and final bend stresses, respectively. The axial error bar is due to deviation in the unirradiated curvature radius.

Table 3. Summary of results of BSR experiments. Numbers in parentheses represent standard deviations

Irradiation creep

Materials	Temperature [°C]	Dose [dpa]	Number of evaluated curvature	Range of initial stress [MPa]	Average BSR ratio	Apparent stress exponent
HNS	580	0.97	24	468–1318	0.35 (0.06)	0.7
	480	12	11	493–1397	0.08 (0.06)	0.7
	1180	0.97	11	450–1374	0.46 (0.04)	0.9
	1140	12	15	452–1403	0.01 (0.02)	1.0
SA3	580	0.97	15	251–748	0.59 (0.04)	0.7
	1180	0.97	8	197–750	0.51 (0.09)	0.8
	1140	12	15	243–754	0.10 (0.07)	0.9
SYL	580	0.97	23	319–985	0.55 (0.09)	0.5
	480	12	11	298–1075	0.10 (0.07)	0.7
	1180	0.97	10	298–1075	0.61 (0.09)	0.6
	1140	12	17	320–912	0.05 (0.07)	0.9
SYL-iBN	580	0.97	24	362–962	0.51 (0.06)	1.2
	480	12	13	333–1109	0.11 (0.06)	0.9
	1180	0.97	11	312–893	0.56 (0.08)	1.2
	1140	12	15	317–893	0.09 (0.09)	0.7

Thermal creep

Materials	Temperature [°C]	Time [h]	Number of evaluated curvature	Range of initial stress [MPa]	Average BSR ratio	Apparent stress exponent
HNS	1180	240	19	471–1373	0.69 (0.05)	0.7
SA3	1180	240	14	230–750	0.63(0.05)	0.8
SYL	1180	240	10	313–996	0.64 (0.10)	0.6
SYL-iBN	1180	240	17	331–964	0.67 (0.08)	0.8

3.3 Microstructural examination of irradiated materials

Secondary electron micrographs of tensile-stressed areas of fiber surfaces before and after creep experiments are shown in Fig. 8. An important finding is that no cracking was

observed on the surfaces in any condition, even when the initial applied stress exceeded 1 GPa. Therefore, irradiation creep was not associated with cracking introduced by applied stress. In addition, the absence of cracking was confirmed in the other SiC materials using an optical microscope with 1000× magnification.

An interesting feature observed is surface modification during irradiation. The surface roughness of the HNS and SYL-iBN fibers was obviously increased by irradiation, but not by heat treatment at ~1,200°C. On the other hand, insignificant effects of irradiation on the surface morphology were found for SA3 and SYL fibers. The change in the fiber surfaces implies instability of the SiC grains and/or impurity phases: nano-SiC grains and carbon impurity phases for HNS and BN and TiB_2 phases for SYL-iBN.

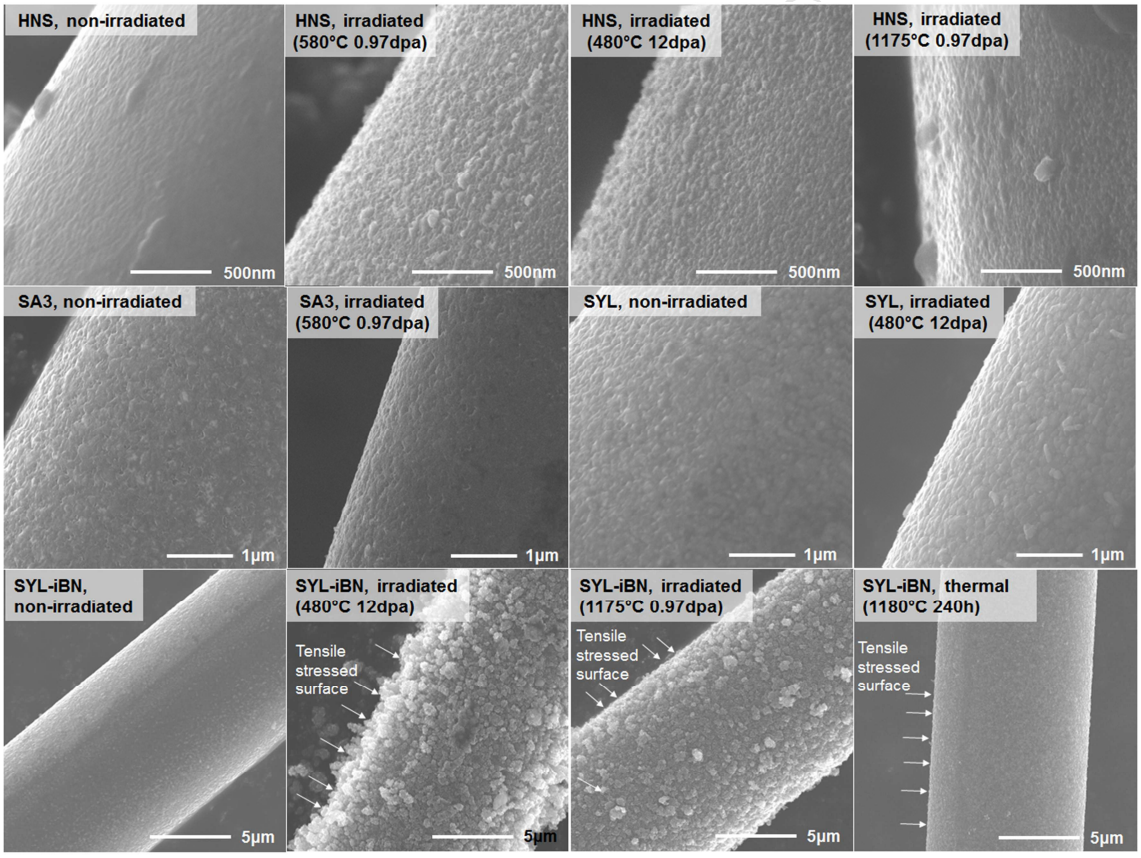

Fig. 8. Secondary electron micrographs of SiC fibers in unirradiated condition and following irradiation and thermal creep experiments. The images were taken from near the tensile stressed surface for the tested specimens unless otherwise indicated.

TEM observation of irradiated RH specimens showed microstructural defects—small clusters, loops, stacking faults, and grain boundaries. The stacking faults and grain boundaries originally existed in RH SiC [5], and no obvious change in these preexisting

defects was confirmed. The dominant irradiation defects were small clusters at 500°C to 11.6 dpa with and without applied stress (Fig. 9). The average size and the number density were ~3 nm and ~1×10^{23} m^{-3}, respectively, independent of the applied stress. The Burgers vector and geometry of those clusters could not be identified in this study. The nature of small defect clusters formed at relatively low temperatures (<~800°C) in SiC is not well understood [20].

Dislocation loops in creep specimens were selectively observed using dark field imaging of streaks. The habit plane is the {111} family of planes. The edge-on loops were taken from the [110] direction, as shown in Figs. 10 and 11. The loop sizes and the number density are summarized in Table 4. A pair of streak images for certain irradiation condition were taken from an identical area, but taken using different streaks indicated in the diffraction pattern. The tensile stress axis is also shown in the images. The line shape of the loop was selected to lie near-perpendicular or parallel to the stress axis in the micrographs. The former loop lies on stressed {111} planes, and the latter lies on unstressed or less stressed {111} planes. The micrographs also show preexisting stacking faults. Following irradiation at 500°C to 11.6 dpa, streaking was barely visible in the diffraction pattern unless preexisting stacking faults were present (Fig. 10a and 10b). The loops with very small number density were observed to be mostly perpendicular to the tensile stress axis. The streaking from the loops was more obvious in the RH specimen irradiated at 440°C to 31 dpa. This is reasonable for observed loops of larger sizes and number densities compared with those seen after 11.6 dpa irradiation. The applied stress during irradiation effectively increased the number density of the loops on the stressed {111} plane; there are more loops in Fig. 10c than in Fig. 10d. The average loop diameter was 7–9 nm, independent of the relationship between the stress axis and the loop-forming plane. A similar anisotropic microstructure was observed at a higher irradiation temperature of 750°C in Fig. 11: the applied stress increased the number density of the loops on the stressed {111} planes and did not significantly affect the loop size. The number density of loops at this temperature was larger than at 440–500°C. Note that the dislocation loops were the dominant defect species compared with the small defect clusters seen by TEM for 750°C irradiation.

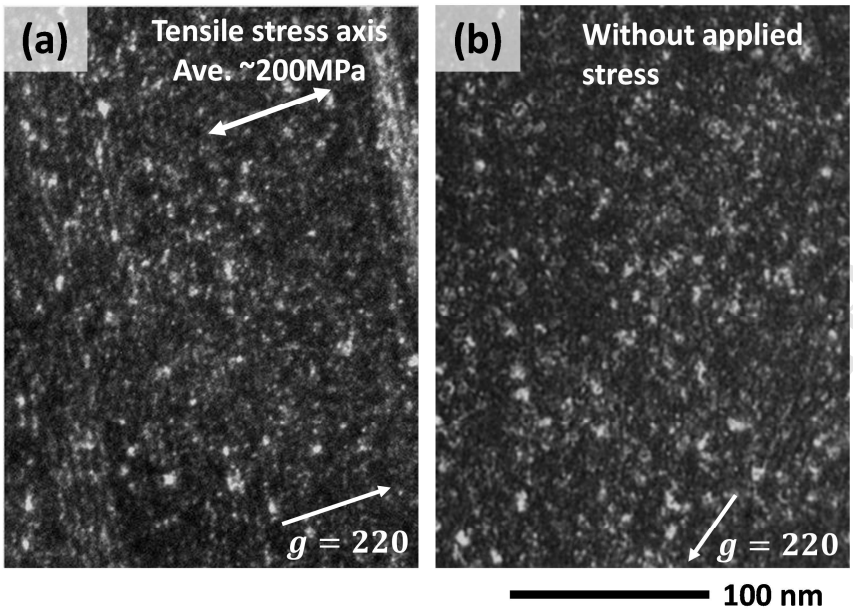

Fig. 9. Weak-beam dark-field images of RH SiC specimen irradiated at 500°C to 11.6 dpa with applied stress (a) and without stress (b). Both images were taken from the near [110] direction. The imaging conditions and stress axes for the creep specimens are indicated in the micrographs.

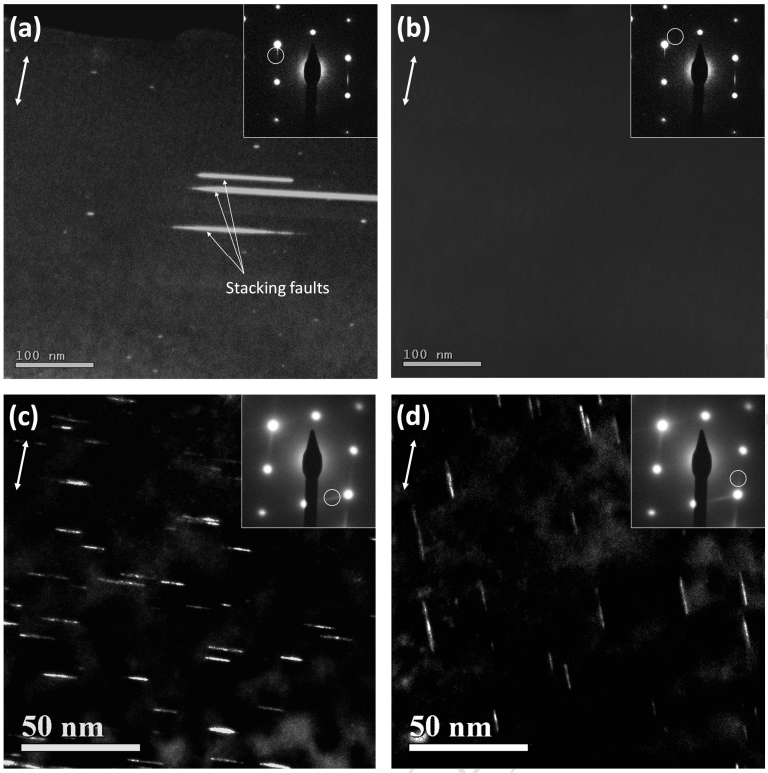

Fig. 10. Edge-on dislocation loops on the {111} planes in the tensile side of an RH SiC specimen irradiated at 500°C to 11.6 dpa (a and b) or at 440°C to 31 dpa (c and d). The stress axis is indicated in the images. The loops are near perpendicular to the stress axis (a and c) or parallel to the stress axis (b and d). Note that the stacking fault is a preexisting defect.

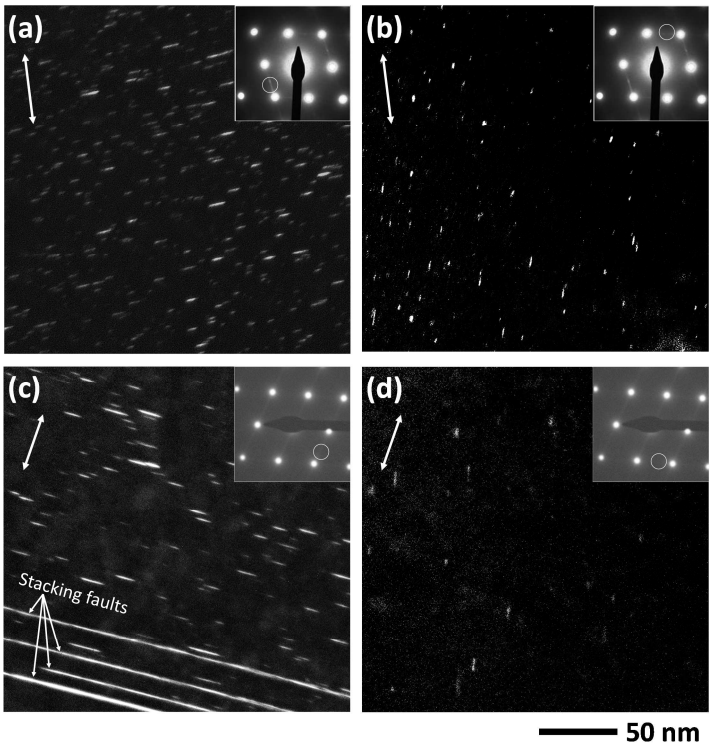

Fig. 11. Edge-on dislocation loops on {111} planes in the tensile side of an RH SiC specimen irradiated at 750°C to 10 dpa (a and b) or 29 dpa (c and d). The stress axis is indicated in the images. The loop lines are near perpendicular to the stress axis (a and c) or parallel to the stress axis (b and d). Note that the stacking fault is a preexisting defect.

Table 4 Summary of microstructural data

Analyzed micrographs	Fig. 10 (a) (b)	Fig. 10 (c) (d)	Fig. 11 (a) (b)	Fig. 11 (c) (d)
Irradiation condition	500°C/11.6dpa	440°C/31.0dpa	750°C/9.7dpa	750°C/29.0dpa
Initial/final stress [MPa]	260/130	220/40	260/100	210/30
Average loop size [nm]				
Zero stressed plane	<~1	6.9	3.2	5.0
Stressed plane	3.5	8.6	5.1	7.5
Loop number density [m^{-3}]				
Zero stressed plane	$<1\times10^{21}$	3.8×10^{22}	2.8×10^{22}	1.6×10^{22}
Stressed plane	2.1×10^{21}	5.6×10^{22}	1.0×10^{23}	1.6×10^{23}

Estimated swelling By loop	~1×10^{-6}	3.9×10^{-4}	2.1×10^{-4}	1.8×10^{-3}
Macroscopic Swelling	1.4×10^{-2}	1.4×10^{-2}	7.3×10^{-3}	8.2×10^{-3}

4. Discussion

4.1 Apparent irradiation creep rate of SiC materials

The creep coefficient, which is normalized creep strain with respect to stress and neutron fluence, is used to indicate creep rate and to compare the creep behavior of different materials [21]. The instantaneous creep coefficient (K) is defined by

$$K \cong \frac{\varepsilon_2 - \varepsilon_1}{\sigma(\gamma_2 - \gamma_1)} \quad , \tag{3}$$

where γ_1 and γ_2 ($\gamma_1 < \gamma_2$) are neutron fluences, σ is average stress during irradiation, and ε_1 and ε_2 are irradiation creep strains following irradiation to fluences of γ_1 and γ_2, respectively. The coefficient is inversely proportional to stress in Eq. (3), which is reasonable because the stress exponents of SiC materials were approximately unity in most cases.

Figure 12 shows the fluence dependence of the instantaneous creep coefficient of the SiC materials. The vertical error bars indicate one standard deviation. The highest and lowest horizontal error bars indicate the fluence of γ_1 and γ_2 for each data point, respectively. The creep coefficient at low neutron fluence was obtained in previous studies [5, 6]. Figure 12 also shows the curves giving the creep behavior calculated by mechanistic models. The transient creep of CVD SiC and sintered SiC materials is described using swelling-coupled creep and logarithmic creep, respectively [5, 6]. The swelling-creep coupling values were expressed as products of the swelling coupling coefficient, applied stress, and swelling rate. Logarithmic creep is commonly observed in metals and ceramics in the transient stage of thermal creep. The creep rate is proportional to t^{-1} where t is time. The logarithmic creep of the sintered SiC is expressed as $K = A\varphi^{-1}$ [dpa MPa]$^{-1}$, where φ is the neutron fluence. The constant, A (= 2×10^{-7} in this study), is a fitting parameter. The behaviors of simultaneous transient creep (swelling coupling or logarithmic creep) and secondary creep with a constant creep coefficient of $K = 1\times10^{-7}$ or 2×10^{-7} [dpa MPa]$^{-1}$ are also shown in the graph.

The creep coefficients of RH, CT, and 4H SiC decreased rapidly with increasing fluence in the transient creep regime up to ~1 dpa, and then the creep coefficients appeared to be constant at ~1×10^{-7} [MPa^{-1} dpa^{-1}] or to become very small, depending on the material type and irradiation temperature (Fig. 12a). The swelling-creep coupling model is a good description of the initial transient creep behavior of CVD SiC materials up to ~1 dpa, as reported in [5]. However, this model cannot explain the creep behavior at higher fluence, which indicates the presence of secondary creep. Additional creep with a constant creep rate of 1×10^{-7} [MPa^{-1} dpa^{-1}] reasonably describes the overall creep behavior, especially for RH SiC at 380–790°C up to 30 dpa. The fluence dependence of the creep coefficients of NT1 and NT2 is similar to that of CVD SiC: a significant reduction with increasing fluence up to ~1 dpa and an apparent steady state value of ~2×10^{-7} [MPa^{-1} dpa^{-1}] at higher fluence. The creep coefficients are slightly larger than for CVD SiC but are within the same order under both low- and high-dose irradiations, as shown in Fig. 12b. The transient creep may be explained as logarithmic creep, as previously discussed [6]. Although the logarithmic creep cannot describe the creep behavior up to 30 dpa, simultaneous transient creep (logarithmic creep) and secondary creep at 2×10^{-7} [MPa^{-1} dpa^{-1}] reasonably fit the creep behavior up to 30 dpa. The creep coefficient of SiC fibers follows the trend of the NT1 and NT2 materials rather than CVD SiC. No significant difference in fluence-dependent creep coefficient was observed between them. In summary, the radiation creep behavior of various SiC materials can be explained using simultaneous transient and secondary creep, and the creep coefficients are on the order of ~10^{-7} [MPa^{-1} dpa^{-1}] or less at 380–790°C above 1 dpa.

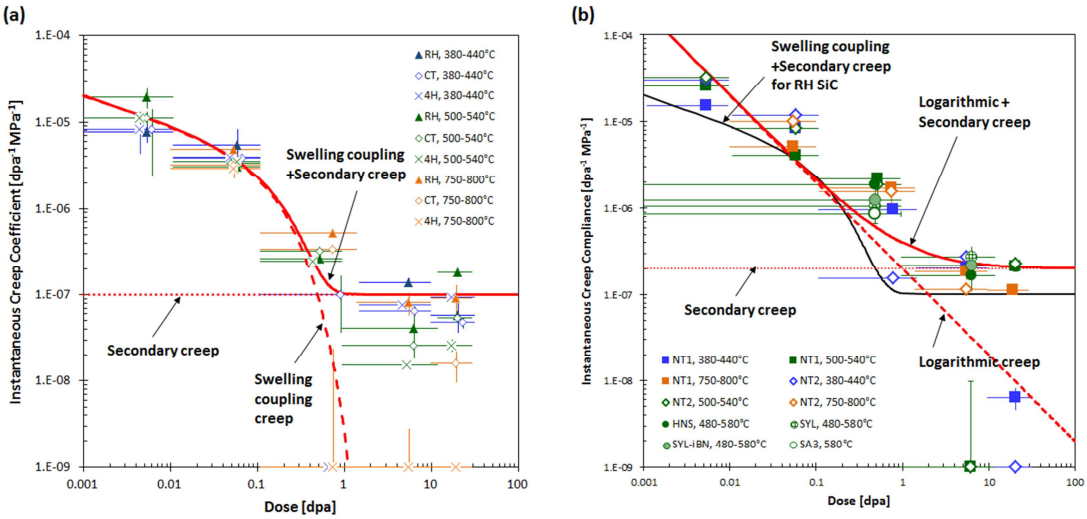

Fig. 12. Neutron dose dependence of instantaneous creep coefficients of CVD SiC materials (a) and nanopowder sintered SiC and SiC fibers (b). The coefficients of CVD SiC and

nanopowder sintered SiC for low dose (<~1 dpa) were obtained in previous studies [5, 6]. Behavior based on creep models such as transient creep (swelling-coupled creep or logarithmic creep) and simultaneous transient and secondary creep is also shown. The data points on 1×10^{-9} [dpa MPa]$^{-1}$ in (a) are actually below that number.

Creep behavior based on the models was also compared with the fluence dependence of BSR ratios in Fig. 13. Simultaneous swelling-coupled creep and secondary creep at 1×10^{-7} [MPa^{-1} dpa^{-1}] reasonably explain the fluence-dependent BSR ratios of RH SiC at 380–790°C in Fig. 13a, in addition to the creep coefficient in Fig. 12a. Regarding CT and 4H SiC materials, the temperature dependence of BSR creep behavior is clearly shown in Fig. 13b. The secondary creep rate of CT and 4H is on the order of 10^{-8} [MPa^{-1} dpa^{-1}] up to 540°C. At 750–790°C, there did not appear to be any creep in CT and 4H SiC beyond ~1 dpa. This differential creep behavior among CVD SiC materials is discussed in Section 4.2.

The fluence dependence of the BSR ratios of NT1 and NT2 is apparently explained by the simultaneous logarithmic creep and secondary creep at 2×10^{-7} [MPa^{-1} dpa^{-1}] rather than by the model used for CVD SiC, as shown in Fig. 13c. This model is also a possible explanation of the creep behavior of the SiC fibers and composite, although the model did not completely fit the trends.

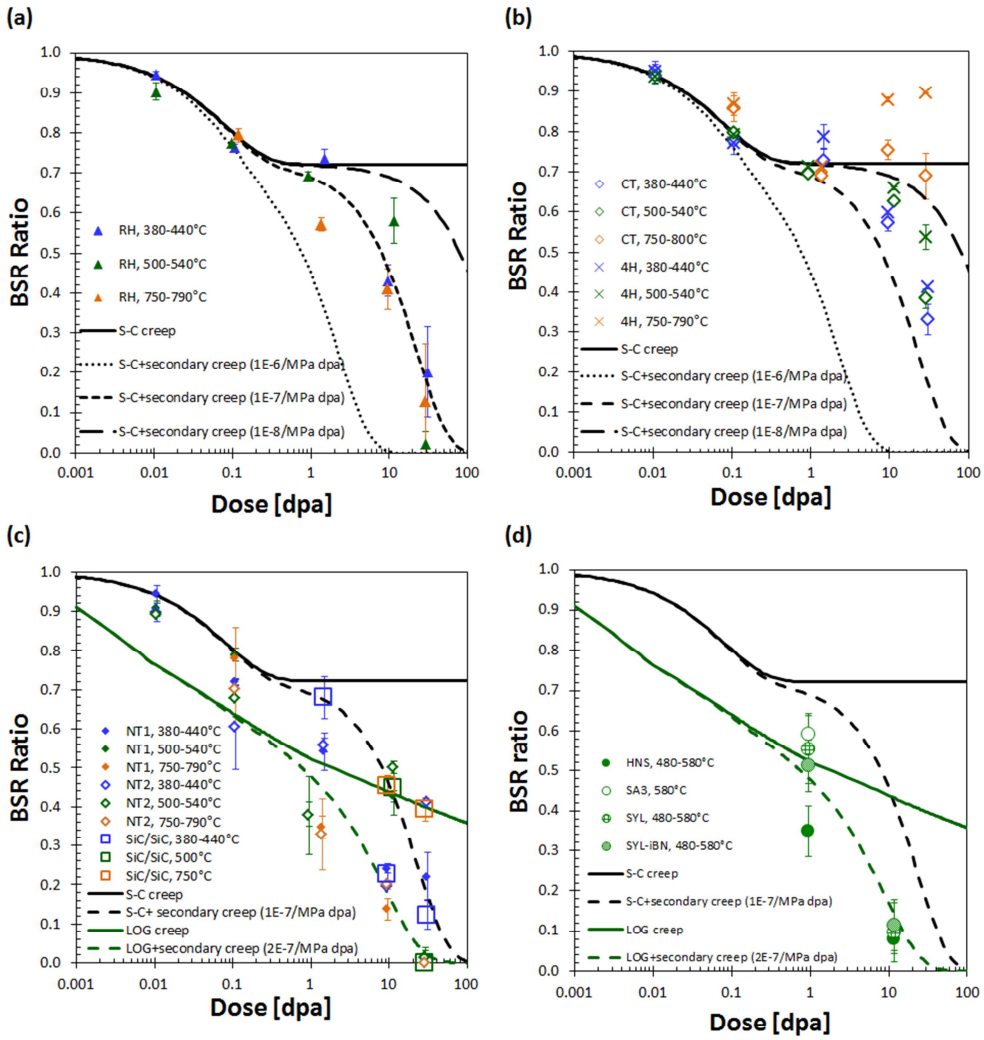

Fig. 13. Dose dependence of BSR ratios of SiC materials: RH (a); CT and 4H (b); NT1, NT2 and SiC/SiC (c); and HNS, SA3, SYL, and SYL-iBN (d). The error bars indicate standard deviations. Trend lines show BSR creep behavior based on creep models, including swelling-coupled (S-C) creep, logarithmic (LOG) creep, and simultaneous S-C or LOG creep with the secondary creep with the constant creep coefficient. Data for most of the bulk specimens at less than ~1 dpa were obtained in previous studies [5, 6].

4.2 Underlying mechanism of post-transient creep

4.2.1 CVD SiC materials

Since transient irradiation creep of CVD SiC materials is believed to be caused by anisotropic swelling [5], swelling can also be a key to understanding the mechanism of post-transient creep. Figure 14 shows the correlation between volumetric swelling and

irradiation creep strain normalized to the average applied stress during irradiation. A linear relationship between swelling and normalized creep strain was obtained for the CVD SiC materials up to ~1 dpa, as reported previously [5]. This leads to the conclusion that transient creep is caused by anisotropic swelling evolution. In the post-transient regime of RH SiC, the swelling saturated, which is a common phenomenon in the point defect swelling regime at less than ~1000°C [17]; but creep still operated independently of swelling. Therefore, post-transient creep may not be explained simply by anisotropic swelling growth. The mechanism of irradiation creep is discussed based on anisotropic microstructural evolution under applied stress. Anisotropy was found in dislocation loop formation on {111} planes in this study. Those relatively larger loops formed in irradiated SiC are likely Frank faulted interstitial loops [20, 22], with a larger number of Frank loops on the stressed planes compared with less stressed planes. This is in clearly seen in Figs. 10 and 11 and was also found in the early stage of the irradiation under an applied stress [20, 25]. Since the formation of Frank loops from interstitials is equivalent to the formation of additional planes, the higher number density of the loops perpendicular to the applied tensile stress axis resulted in a greater increase in length in the direction of the tensile stress axis, i.e., creep strain. This phenomenon is typical for the creep mechanism owing to the stress-induced preferential nucleation of loops (SIPN) [23] or stress-induced preferential absorption (SIPA) of interstitials [24]. Therefore, the irradiation creep of RH SiC can be phenomenologically explained by the SIPN and/or SIPA mechanism.

The creep mechanism in the post-transient regime can also be discussed based on changes in anisotropic loop formation from 10 to 30 dpa. As shown in Figs. 10 and 11, the features of the microstructural evolution during the secondary creep regime were (1) the larger number of loops on the stressed planes compared with the less stressed planes, (2) the increase in loop density with increasing fluence at 440–500°C, and (3) the growth of the loops at 440–750°C. Phenomenon 1 has already been observed in the transient creep regime, which is a typical feature of SIPN and/or SIPA. Phenomenon 2 can be explained by the formation of a new loop by SIPN and/or the growth of small clusters via SIPA. Phenomenon 3 can be caused by SIPA. Thus, both SIPN and SIPA are possible creep mechanisms in the secondary creep regime. The stress exponent of near unity in this study is consistent with these mechanisms [23, 24]. Although the previous paragraph qualitatively discussed the creep mechanism, it is still difficult to quantitatively explain irradiation creep strain in SiC. This is because the observed dislocation loops account for only a small fraction of the dimensional changes, i.e., the swelling of bulk SiC. Assuming stoichiometric Frank interstitial loops are formed in SiC, observed loops account for up to 20 % of macroscopic swelling (Table 4). Previous studies on irradiation creep in SiC at lower neutron fluences indicate the anisotropic formation of

TEM-invisible defect clusters, and they significantly contribute to the creep strain [5, 20]. That is also the case for this study. Since a recent ion irradiation study indicates that the orientation of dislocation loops and self-interstitial atom clusters is determined at a very early stage of irradiation [25], the observed formation of relatively large anisotropic loops indicates the possible anisotropic formation of small defect clusters at the early stages of irradiation. Therefore, this study indirectly shows that the anisotropic formation of small defect clusters as a result of applied stress makes a significant contribution to irradiation creep strain in RH SiC.

In the case of CT and 4H SiC, the creep mechanism is expected to be similar to that of RH SiC unless microstructural differences of the starting material affect the irradiation creep. The creep-swelling relationship of CT and 4H follows the trend of RH SiC, and the swelling was very similar for the three types of CVD SiC up to 540°C, as shown in Fig. 14. Therefore, a similar creep mechanism caused by radiation defects is expected for CT and 4H materials. Swelling was also similar between the CVD materials at 750°C, but the creep-swelling relationship of CT and 4H deviates from the trend of RH because of their smaller creep strains. This result indicates that the defect evolution causing swelling was basically similar to that in CVD SiC materials, and it indicates that the microstructural anisotropy in the unirradiated condition strongly affected the creep behavior at 750°C. The effects of the initial microstructure on irradiation creep are discussed in the next section.

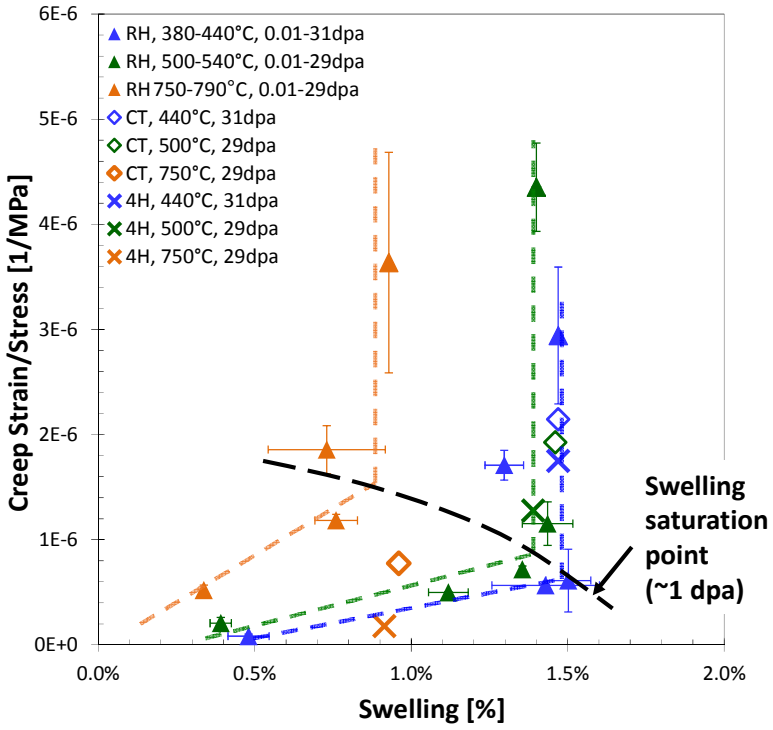

Fig. 14. Correlation between volumetric swelling and stress-normalized irradiation creep strain in CVD SiC materials. Low-dose data up to 1.5 dpa were obtained in a previous study [5]. Colored dotted lines show the trend for RH SiC.

4.2.2 Effect of starting microstructure on creep of CVD SiC, sintered SiC, and SiC fibers

The differential creep behavior among various SiC materials in Figs. 12, 13, and 14 indicates that the starting microstructure affected creep behavior in the post-transient regime. Microstructural differences among CVD SiC, sintered SiC, and SiC fibers included grain size and impurity phases located mainly between grains. Therefore, differential creep behavior is suspected to be caused by grain boundary–related mechanisms. Figure 15 shows instantaneous creep coefficients plotted against grain size for CVD SiC, sintered SiC, and SiC fibers. The grain size of 4H SiC is assumed to be 40 mm, which is the length of the strip specimen. Irradiation temperature affected the grain-size dependence of the creep coefficient as follows. The creep was independent of grain size at ~400°C. Above this temperature, the SiC with smaller grains exhibited a larger creep coefficient, which was more significant at higher irradiation temperatures. Although the structures of grain boundaries are different depending on the material, the smaller grains led to the greater contribution of grain boundaries to irradiation creep.

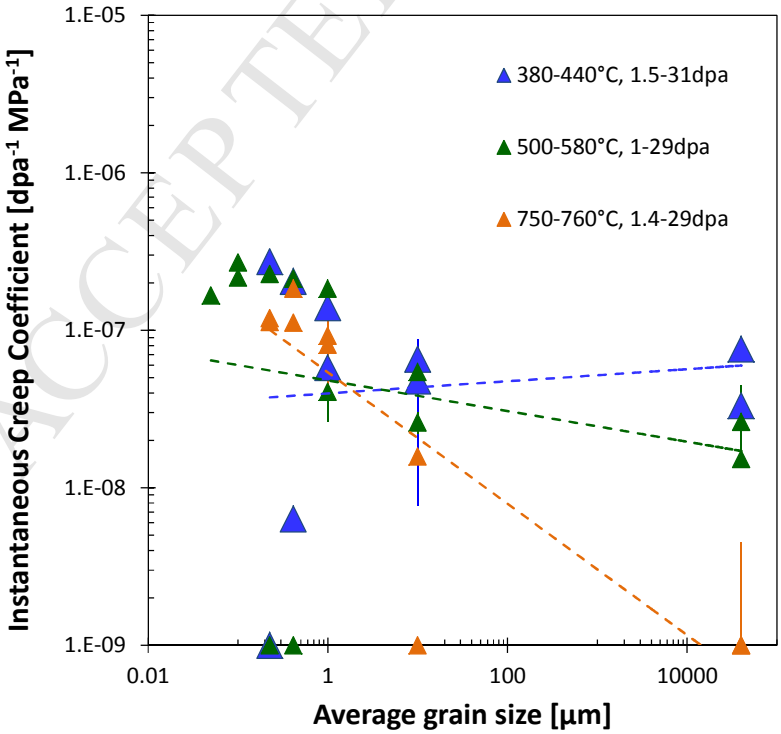

Fig. 15. Grain-size dependence of instantaneous creep coefficient for various SiC materials. Trend lines fitted using a power law distribution are also shown. The data points on 1×10^{-9} [dpa MPa]$^{-1}$ are actually below that number.

Microstructural differences among CVD SiC materials include not only grain size but also material anisotropy. Katoh et al. investigated the details of microstructures in RH and CT and concluded that the incoherent grain boundaries lacking in CT and 4H contributed to the irradiation creep at high temperatures and low neutron fluence [5]. This is also a possible explanation for the larger creep strain of RH compared with CT and 4H at higher fluence. Therefore, the creep strain of RH at 750°C, which cannot be fully explained by TEM microstructures, is possibly affected by grain boundary sliding.

Grain-boundary sliding of NT1 and NT2 materials is considered to be related to the secondary phases (mostly Y-Al oxides) existing in grain boundaries and grain pockets, which were reported in the low-dose radiation creep experiment [6]. If that is also the case at higher doses, NT2 with finer grains and a larger amount of secondary phases should exhibit larger creep than NT1. However, the relationship of creep strain between NT1 and NT2 was not clear under irradiation to >~10dpa. The creep mechanism of sintered SiC may not be easily explained by grain boundary sliding. Further analysis of the high-dose creep of NT1 and NT2 using TEM observation has not been conducted because of the difficulty of capturing the very small creep strain.

Secondary phases in SiC fibers are also expected to contribute to grain boundary sliding under radiation. The common secondary phases for HMS, SA3, SYL, and SYL-iBN are free carbon at grain boundaries and triple junctions. Note that the morphologies of the carbon phase, such as distribution and structure, may be different among them. Additional titanium diborides were contained in SYL and SYL-iBN. Since the BSR behavior of SYL and SYL-iBN was similar to that of SA3, as shown in Fig. 13d, the diborides phase appeared to have an insignificant effect on irradiation creep at 580°C up to 1 dpa. On the other hand, HNS exhibited a larger creep than the other materials for this irradiation condition. Finer grains of HNS and/or carbon phases are expected to contribute to creep behavior. To the best of our knowledge, neutron irradiation creep of SiC fibers has not yet been investigated by other researchers. Instead, ion irradiation was used to investigate creep in SiC fibers. Scholz reported the creep behavior of SCS-6 fiber at 600°C at 0.04 dpa using a torsion creep experiment with proton irradiation [9]. The reported creep coefficient for steady-state creep (3×10^{-5} [MPa dpa]$^{-1}$) was more than two orders of magnitude larger than the value for the SiC fibers at 1–10 dpa found in this work. This discrepancy is possibly caused by (1) lower

creep resistance of SCS-6 fiber, (2) "apparent" steady-state creep in Scholz's experiment, and (3) difference in the displacement damage rate and test method (torsion shear vs. BSR).

The irradiation creep behavior of SiC/SiC can be discussed via a relative comparison of the BSR ratios among SiC materials in Fig. 13. The NT1 and NT2 materials can be reference materials for the matrix phase of SiC/SiC because of the similarity in the microstructural features exhibiting submicron grains and oxide phases at grain boundaries and pockets. The SA3 fiber is the reference for the fiber in the composite. The BSR ratio of SiC/SiC is expected to be similar to that of one of the reference materials if the creep of one constituent in SiC/SiC governs the creep of the composite. Otherwise, other factors, including creep of the carbon interphase, creep of segregated secondary phases, and internal residual stress originally introduced during processing, may affect the creep behavior. Note that the stress transfer among the fiber, matrix, and interphase due to differential creep resistance is expected to be insignificant for BSR experiments with constant strain applied to the constituents, although it can be significant in tensile creep experiments and can strongly affect the creep behavior of SiC composites [26]. The BSR ratios of SiC/SiC were similar to that of at least one of the reference materials at 380–500°C to more than 1 dpa, indicating the composite constituent affecting the creep of SiC/SiC. On the other hand, SiC/SiC was more creep-resistant than sintered SiC at 800°C, as shown in Fig. 13d. The important finding is that SiC/SiC did not show significant irradiation creep similar to that of the other SiC materials. Creep life during irradiation needs to be evaluated in further creep experiments with constant applied stress, since creep rapture cannot be achieved by BSR experiments.

4.3 Comparison of secondary irradiation creep among SiC and other nuclear materials

We found that the instantaneous creep coefficient was ~1×10^{-7} [MPa dpa]$^{-1}$ at ~400 to ~750°C to ~1–30 dpa for all the SiC materials except for the SiC with coarse grains at ~750°C (Fig. 12). That creep coefficient is compared with those of the metals in Fig. 16. The post-transient irradiation creep was investigated for zirconium alloys [27, 28], vanadium alloy (V-4Cr-4Ti) [29], austenitic stainless steels including 316 and 304 [30, 31, 32], oxide-dispersion-strengthened (ODS) ferritic steels (MA957 and HT9) [33], and ferritic/martensitic steels (F82H and JLF-1) [34, 35]. Those irradiation temperatures ranged from ~300 to ~700°C. The irradiation creep was investigated using a pressurized tube method for all the materials other than SiC. The stress exponents of those materials are reported to be between one and two. Although the test method, irradiation conditions, and stress exponents were different, the significant differences in the creep coefficient between SiC and the other materials can be discussed. The creep coefficient of the zirconium

alloys was ~1×10^{-5} [MPa dpa]$^{-1}$. A slightly smaller creep coefficient of ~5 × 10^{-6} [MPa dpa]$^{-1}$ was obtained for the specific vanadium alloy. A much smaller creep coefficient of ~1×10^{-6} [MPa dpa]$^{-1}$ was typical for the austenitic stainless, ODS, and ferritic/martensitic steels. The creep coefficients of the SiC materials were approximately one order smaller than the coefficients for those steels. Therefore, the creep coefficients of the SiC materials are extremely small compared with those of the other nuclear materials. Although the smaller creep coefficient does not necessarily indicate a longer creep lifetime, it can be concluded that the smaller creep coefficient contributes to higher dimensional stability. In the case of the high-purity CVD SiC, the saturation of swelling above ~1 dpa (Fig. 14) in addition to the small creep coefficient makes the material more dimensionally stable in the irradiation environment than the metals.

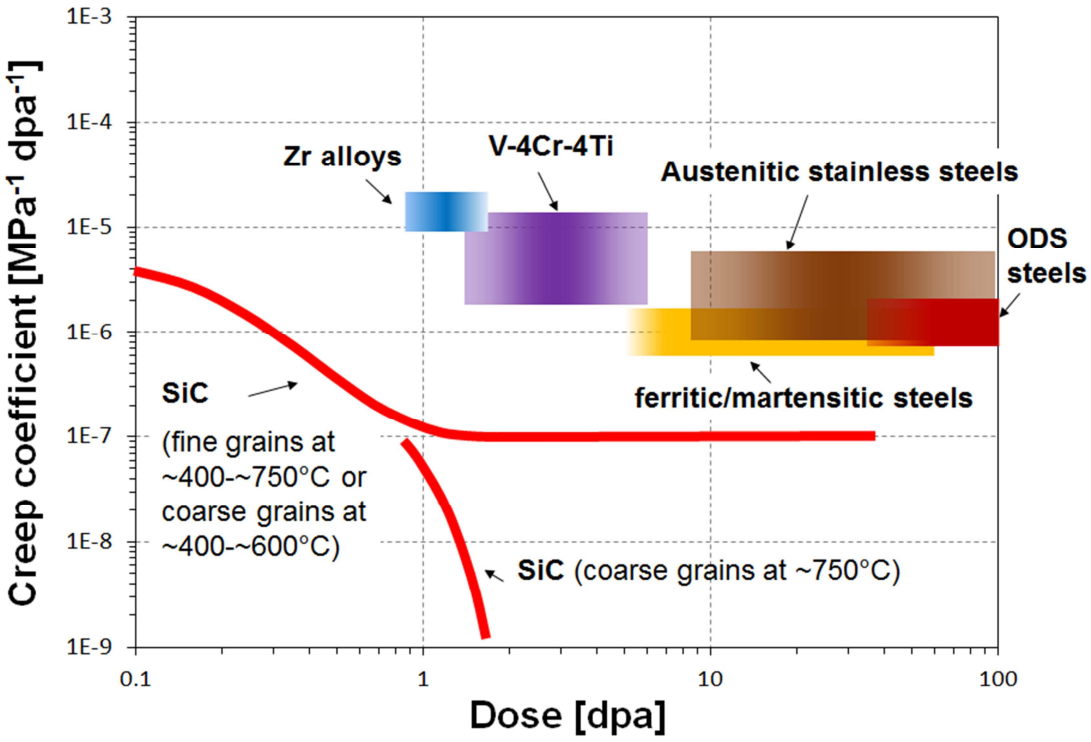

Fig. 16 Comparison of typical creep coefficients among different nuclear materials. The data for the metals were reported in elsewhere [27–35].

5. Conclusions

The irradiation creep of various SiC materials was evaluated and analyzed following irradiation at 380–1180°C up to 31 dpa. The findings in this study are as follows.

1) Creep operates in CVD SiC, sintered SiC ceramics, SiC fibers, and NITE SiC composites under irradiation to more than ~1 dpa, which is beyond the transient creep region of CVD SiC.
2) The apparent stress exponent of irradiation creep is approximately unity during irradiation to high neutron fluences in most cases. The stress exponent of the SiC fibers tends to be slightly smaller than unity.
3) The creep behavior of CVD SiC and sintered SiC can be explained as simultaneous transient creep and secondary creep at ~400 to ~800°C.
4) The instantaneous creep coefficients of CVD SiC, sintered SiC, and SiC fibers are $1–2\times10^{-7}$ $[\text{MPa dpa}]^{-1}$ for irradiation fluences of 1–30 dpa. The NITE SiC composite exhibited similar or slightly better creep resistance compared with sintered SiC and SiC fibers in a bend stress relaxation configuration with initial stress of up to 140 MPa.
5) Applied stress during irradiation increased the number density of loops on stressed {111} planes in polycrystalline fine-grained 3C SiC. The loops grew slightly with increasing fluence. The anisotropic loop formation and loop growth accounts for part of the macroscopic creep strain, which can be explained by the SIPN and/or SIPA mechanisms.
6) The effects of starting microstructure on irradiation creep—including grain size, grain anisotropy, and secondary phases at grain boundaries and pockets—increased with increasing irradiation temperature.
7) The dimensional stability of CVD SiC materials under an irradiation environment is superior to the stability of nuclear alloys because of the smaller creep coefficient and the saturation of the swelling.

Acknowledgements

This work was supported by the Office of Fusion Energy Sciences, U.S. Department of Energy, under contract DE-C05-00OR22725 with UT-Battelle, LLC, and the US–Japan TITAN Collaboration on Fusion Blanket Technology and Materials. Research was supported in part by the High Flux Isotope Reactor, which is sponsored by the Office of Basic Energy Sciences, U.S. Department of Energy. The authors would like to gratefully acknowledge contributions to pre- and post-irradiation experiments from F. C. Montgomery, C. M. Silva, A. M. Williams, P. S. Tedder, C. Shih and M. R. McAlister at Oak Ridge National Laboratory, and M. Fukuda at Tohoku University.

References

[1] Y. Katoh, K. Ozawa, C. Shih, T. Nozawa, R.J. Shinavski, A. Hasegawa, L.L. Snead, J. Nucl. Mater., 448 (2014) 448–476.

[2] Y. Katoh, L.L. Snead, C.H. Henager Jr., T. Nozawa, T. Hinoki, A. Ivekovic´, S. Novak, S.M. Gonzalez de Vicente, J. Nucl. Mater., 455 (2014) 378–379.

[3] R.J. Price, Nucl. Technol. 35 (1977) 320–336.

[4]Y. Katoh, L.L. Snead, T. Hinoki, S. Kondo, A. Kohyama, J. Nucl. Mater., 367–370 (2007) 758–763.

[5] Y. Katoh, L.L. Snead, C.M. Parish, T. Hinoki, J. Nucl. Mater., 434 (2013) 141.

[6] T. Koyanagi, K. Shimoda, S. Kondo, T. Hinoki, K. Ozawa, Y. Katoh, J. Nucl. Mater., 455 (2014) 73–80.

[7] J. Huguet-Garcia, A. Jankowiak, S. Miro, Y. Serruys, J.M. Costantini, Nuclear Instruments and Methods in Physics Research B, 327 (2014) 93.

[8] R. Scholz, J. Nucl. Mater., 258 (1998) 1533.

[9] R. Scholz, G.E. Youngblood, J. Nucl. Mater., 283 (2000) 372.

[10] J. Huguet-Garcia, A. Jankowiak, S. Miro, Y. Serruys, J.M. Costantini, Nuclear Instruments and Methods in Physics Research B, 327 (2014) 93–98.

[11] J. Huguet-Garcia, A. Jankowiak, S. Miro, T. Vandenberghe, C. Grygiel, I. Monnet, J.M. Costantini, J. Mater. Res., 30[09] (2015) 1572–k1582.

[12] G.N. Morscher, J.A. Dicarlo, J. Am. Ceram. Soc., 75 (1992) 136.

[13] Y. Katoh, S.M. Dong, A. Kohyama, Fusion Eng. Des., 61‑62 (2002) 723–731.

[14] K. Shimoda, J.S. Park, T. Hinoki, A. Kohyama, J. Nucl. Mater., 386–388 (2009) 634–638.

[15] H.M. Yun, J.Z. Gyekenyesi, Y.L. Chen, D.R. Wheeler, J.A. DiCarlo, Ceram. Sci. Proc., 22 (2001) 521–531.

[16] C. Sauder, J. Lamon, J. Am. Ceram. Soc., 90 [4] (2007) 1146–1156.

[17] L.L. Snead, T. Nozawa, Y. Katoh, T.-S. Byun, S. Kondo, D.A. Petti, J. Nucl. Mater., 371 (2007) 329.

[18] A.A. Campbell, W.D. Porter, Y. Katoh, L.L. Snead, Nucl. Instrum. Meth. B, 370 (2016) 49.

[19] V.V. Pujar, J.D. Cawley, J. Am. Ceram. Soc., 78[3] (1995) 774–782.

[20] Y. Katoh, S. Kondo, L.L. Snead, J. Nucl. Mater., 382 (2008) 170–175.

[21] K. Ehrlich, J. Nucl. Mater., 100 (1981) 149.

[22] Y. Katoh, N. Hashimoto, S. Kondo, L.L. Snead, A. Kohyama, J. Nucl. Mater., 351 (2006) 228–240.

[23] A.D. Brailsford, R. Bulloug, Philos. Mag., 27[1] (1973) 49.

[24] P. T. Heald, M.V. Speight, Philos. Mag., 29[5] (1974) 1075.

[25] S. Kondo, T. Koyanagi, T. Hinoki, J. Nucl. Mater., 448 (2013) 487.

[26] A.G. Evans, C. Weber, Mater. Sci. Eng., A208 (1996) 1–6.

[27] E.F. Ibrahim, R.A. Holt, J. Nucl. Mater., 91 (1980) 311.

[28] V. Fidleris, J. Nucl. Mater.. 159 (1988) 22.

[29] M. Li, D.T. Hoelzer, M.L. Grossbeck, A.F. Rowcliffe, S.J. Zinkle, R.J. Kurtz, J. Nucl. Mater.. 386 (2009) 618.

[30] F.A. Garner, D.L. Porter, J. Nucl. Mater., 155 (1988) 1006.

[31] D.L. Porter, G.D. Hudman, F.A. Garner, J. Nucl. Mater., 179 (1991) 581.

[32] K. Egrlich (1981) J. Nucl. Mater., 100 (1981) 149.

[33] M.B. Toloczko, D.S. Gelles, F.A. Garner, R.J. Kurtz, K. Abe, J. Nucl. Mater., 329 (2008) 352.

[34] M. Ando, M. Li, H. Tanigawa, M.L. Grossbeck, S. Kim, T. Sawai, K. Shiba, Y. Kohno, A. Kohyama, J. Nucl. Mater., 367 (2007) 122.

[35] A. Kohyama, Y. Kohno, K. Asakura, M. Yoshino, C. Namba, C.R. Eiholzer, J. Nucl. Mater., 212 (1994) 751.